Vol. 20 / No. 4

JM3 Journal of Micro/Nanopatterning, Materials, and Metrology

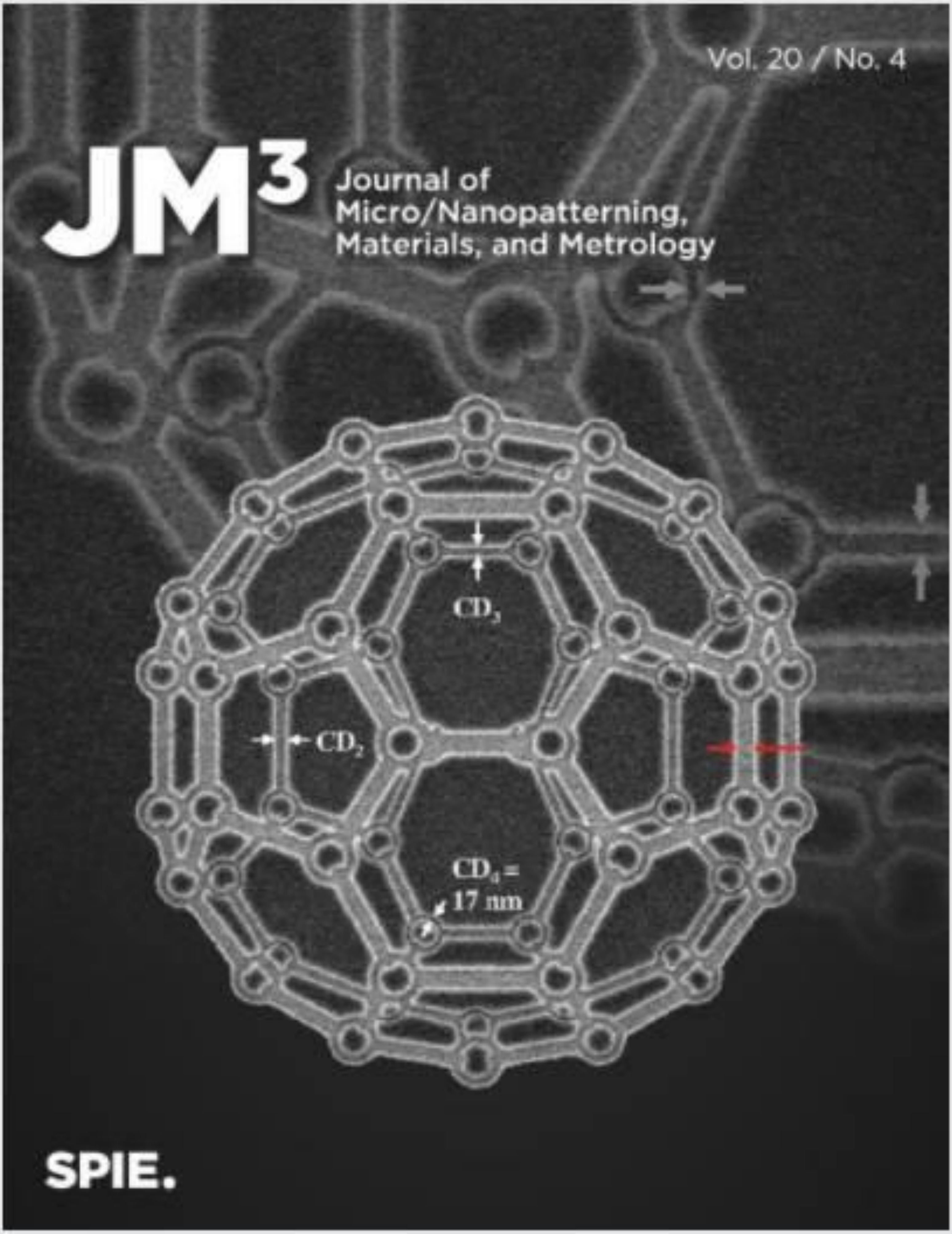

SPIE.

ALL ISSUES

VOL. 20 | 2021

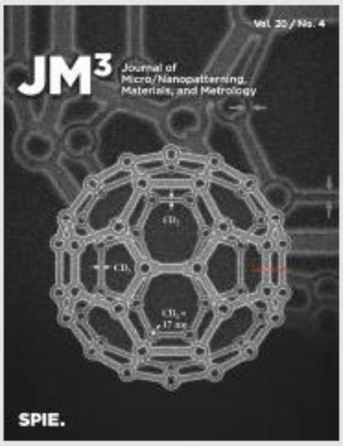

VOL. 20 | NO. 04
October 2021

VOL. 20 | NO. 03
July 2021

VOL. 20 | NO. 02
April 2021

VOL. 20 | NO. 01
January 2021

Journal of Micro/Nanopatterning, Materials, and Metrology

Editor-in-Chief: Harry Levinson, HJL Lithography, USA

The *Journal of Micro/Nanopatterning, Materials, and Metrology* (JM^3) publishes peer-reviewed papers on the core enabling technologies that address the patterning needs of the electronics industry. Formerly the *Journal of Micro/Nanolithography, MEMS, and MOEMS*, the journal's key subject areas include the science, development, and practice of lithographic, computational, etch, and integration technologies. In this context the electronics industry includes but is not limited to integrated circuits and multichip modules, and advanced packaging with features in the submicron regime.

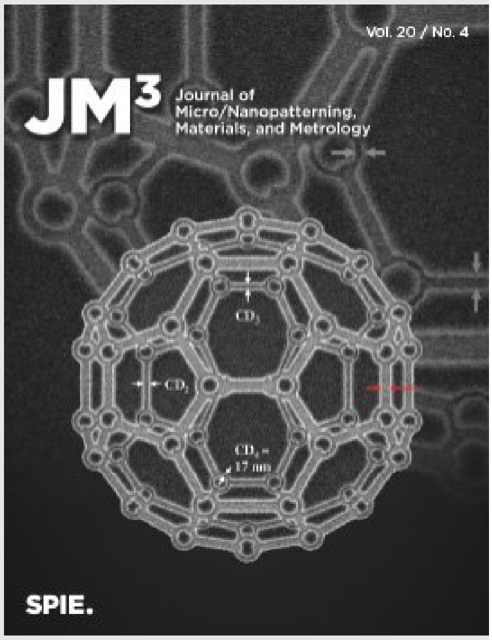

On the cover: The figure is from the paper "Multi-beam mask writer exposure optimization for EUV mask stacks" by P. Hudek et al. in the Special Section on Masks and Lithography in the Era of Multi-beam Mask Writers in Vol. 20, Issue 4.

Multi-beam mask writer exposure optimization for EUV mask stacks

Peter Hudek,[a,*] Michal Jurkovič,[a] Pavlina Choleva,[a] Witold Wroczewski,[a] Masahiro Hashimoto,[b] Kazunori Ono,[b] Toru Fukui,[b] Toshiya Takahashi,[c] and Kotaro Takahashi[c]

[a]IMS Nanofabrication GmbH, Vienna, Austria
[b]HOYA, Nakamaru, Nagasaka-cho, Hokuto-shi, Yamanashi, Japan
[c]FUJIFILM Corporation, Yoshida-cho, Haibara-gun, Shizuoka, Japan

Abstract

Background: EUV lithography is making substantial progress in optimizing (i) tool, (ii) mask blanks, and (iii) resist materials to support the next generation EUV imaging performance. EUV masks use a variety of absorbers and capping layers fabricated on mirroring multi-layer (ML) stacks.

Aim: The highly conformal e-beam resist-patterning process needs to understand the absorbed intensity distribution spread from the electron scattering in the resist/substrate stack, as well as the consecutive radiation-chemical effects induced by the electron energy spread together with the dissolution behavior of the resist.

Approach: We present the results of resist response to 50-keV electron multi-beam exposure based on statistical numerical simulation on different EUV absorbers and reflecting ML stacks directly compared with the numerical lithographic parameters extracted from the experimental resist screening. The experiments were performed with the IMS Nanofabrication Multi-Beam Mask Writer (MBMW) ALPHA tool in a positive Chemically Amplified Resist provided by FUJIFILM, coated on experimental EUV masks with different stack compositions prepared by HOYA.

Results: All input parameters for MBMW corrections were precisely specified to the corresponding absorbed energy distribution signature of the specific EUV stack. Experiments confirmed the necessity to match the model calibration values to each small change in the mask stack composition.

Conclusions: The method was successfully implemented into leading-edge mask writing and resist/substrate/tool testing for achieving the sub-7-nm node at different EUV-mask stacks.

 [DOI: 10.1117/1.JMM.20.4.041402]

Keywords: electron beam lithography; multi-beam mask writer; extreme ultraviolet; mask blank; chemically amplified-resists.

Paper 21032SS received Apr. 8, 2021; accepted for publication Jul. 23, 2021; published online Oct. 28, 2021.

1 Introduction

E-beam lithography (EBL), in general, utilizes a beam of high-energy electrons to provide radiation-chemical changes to the recording medium, typically a thin polymer resist layer coated on a multi-layered (ML) surface of the substrate.

The main goal of e-beam high-end mask writing lithography is now concentrated on printing complex mask patterns on different absorber stacks to enable a highly conformal wafer-level projection of images with high conformity and a sufficient process window in real-time.

*Address all correspondence to Peter Hudek, peter.hudek@ims.co.at

1932-5150/2021/$28.00 © 2021 SPIE

Computational optical modeling for sub-wavelength imaging, using aggressive resolution enhancement technology steps such as inverse-lithography technology, results in curvilinear non-orthogonal geometries on the mask representing the wafer target shape.[1] The highly complicated curvilinear mask pattern geometry, which plays a crucial role in increasing the wafer process window, results in an enormous increase in the number of polygon vertices in the mask layout-data, representing the pattern contours. Other correction methods, minimizing mask process errors, such as the mask process correction (MPC) technique,[2] amplifies this effect, adding more complexity to the mask.

Recently developed multi-beam mask writers (MBMW) by IMS Nanofabrication ("IMS") have become mature for sub-10-nm node applications.[3] Utilizing massively parallel architecture and novel writing strategies, MBMWs handle huge pattern data along with the capability of delivering sufficient exposure dose, including low sensitive (high exposure dose) resists, with reasonable write times.[4] Consequently, the need for an advanced resist characterization technique, dependent on mask-stack material changes in a short-loop, is necessary.

In the case of mask/reticle making for the projection lithographies using short-wavelength EUV photons, the substrate material consists of a specific absorber layer on top of the ML (EUV-mask) deposited on a massive bulk ultra-low thermal expansion substrate. Expecting wafer-level feature dimensions as small as 12-nm half-pitch (hp) and beyond with a single exposure, the most promising candidate for next-generation technology processes is EUV-lithography. The continuous improvement in imaging performance of the EUV-mask[5] still needs fine-tuning in the manufacturing process and materials of both absorber and reflective ML mirror stack.[6–8] MBMW tools are writing high-fidelity patterns independent of mask density and complexity using constant shot-size. Therefore, precise control of the number and position of incident electrons inside the closed pattern contours, taking into account all interacting neighbors, is needed. Thus, changes in substrate material composition directly influence the scattering phenomena of impinging electrons and by that the delivered total aerial dose creating the patterns in the resist film. The resist employed must meet the demand for the highest resolution within the desired write times for leading-edge mask production.

2 Exposure Optimization

The main goal of resist-based lithography has been the precise geometry control and faithful reproduction of the intended pattern for diverse technology processes using a variety of electron-sensitive organic (polymeric) resist materials. This can only be realized if all details of the desired pattern will be irradiated by the optimum intensity required by the particular resist and the specified pre- and post-exposure processes.

The requirement for high resolution and critical dimension (CD)-uniformity may become limited by a combination of:

i. E-beam parameters (acceleration voltage, current density, dose linearity, blur, and beam optical aberrations)
ii. Tool (tool architecture, writing strategy, stage quality, and overall stability);
iii. Electron scattering effects in the resist/substrate;
iv. Resist (composition, radiation-chemical processes, contamination, and outgassing);
v. Pre- and post-exposure processes (coating, baking, and development);
vi. Pattern transfer process into the mask absorber stack.

To use the lithography most effectively, it is useful to understand the physics of electron scattering in various resist/substrate stacks in combination with the radiation-chemical effects in the exposed resist volume. The resolution of EBL is determined mainly by the interaction-range between the electrons and the resist. A highly conformal pattern writing itself needs to use an efficient exposure correction which requires an adequate knowledge and experience base to predict all parasitic effects causing pattern degradation through the lithography process:

i. The molecular structure of the resist (*);

ii. The delocalization of the exposure process, as determined by the range of the Coulomb interaction between the electrons and the resist molecules (*);
iii. The scattering of secondary electrons (SE) into the resist;
iv. Process correlation between aerial image, latent image, and the resulting resist-relief structure;

* The relative behavioral contributions are not well known, but their overall effect can be holistically modeled for a particular resist type and the whole patterning process respectively.

According to numerical evaluation, two main methods can be used for physical modeling of the scattering process: (i) continuous analytical[9–11] or (ii) statistical Monte Carlo methods.[12–14]

2.1 *Tracking e-Trajectories*

The ultimate resolution in EBL is determined by the amount of laterally and back-scattered electrons in the resist from specific target compositions. These interaction events cause parasitic proximity, fogging, local heating, and surface charging effects, defining the accurate pattern CD.

Hence, the electron scattering is the main object of calculations in that field to obtain the absorbed energy density distribution (AEDD) from a point e-beam in the irradiated target volume. AEDD, as a function of position (x, y), is usually modeled using the point-spread function (PSF). PSF is, in this case, PSF for deposited energy, a normalized form of analytically approximated radially symmetrical exposure intensity spread inside the material around the incident direction caused by electron scattering events. In the frequently used Monte Carlo simulation method, a statistical technique for modeling of e-beam radiation effects using the probability distribution of physical events in a material, the PSF for deposited energy in a representative depth of resist is calculated in two main steps:

a. Propagation—tracing the path [Fig. 1(a)] and the distribution of the scattered electrons in ML material [Fig. 2(b)] before escaping or losing their energy, and
b. Deposition—how the energy is transferred from electrons to the material [Figs. 2(c) and 2(d)].

Figure 2(a) shows the schematic cross-section of two out of four samples, chrome-on-glass (CoG) and S3 (EUV mask blank) used in this work. Figures 2(b) and 2(c), illustrate the simulation results, using Casino Software,[15] of these two different resist coated substrate types after a 20-nm diameter e-beam irradiation with 50-keV electrons. The simulation did not include blur from beam shape.

The lateral scattering distance of electrons is directly related to the intensity of the unwanted exposure deposition in the area surrounding a written pattern feature. For high-end processes, all parasitic contributions on the possible final resist image distortion are an issue of increasing concern. The calculated results in Fig. 2 follow the "fast" classical statistical model based on Rutherford differential elastic scattering cross-section and the Bethe's continuously slowing

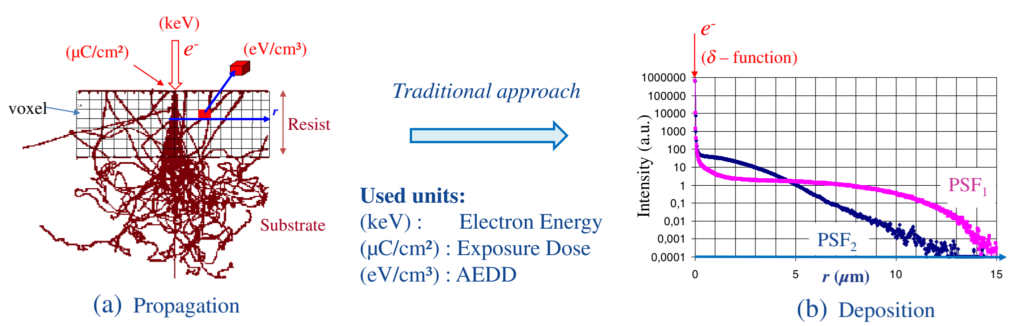

Fig. 1 Monte Carlo simulation method steps: (a) Propagation step—tracing discrete electron scattering paths; (b) Deposition—adding up of energy left in each resist voxel through-thickness of the resist film to calculate the AEDD per voxel.

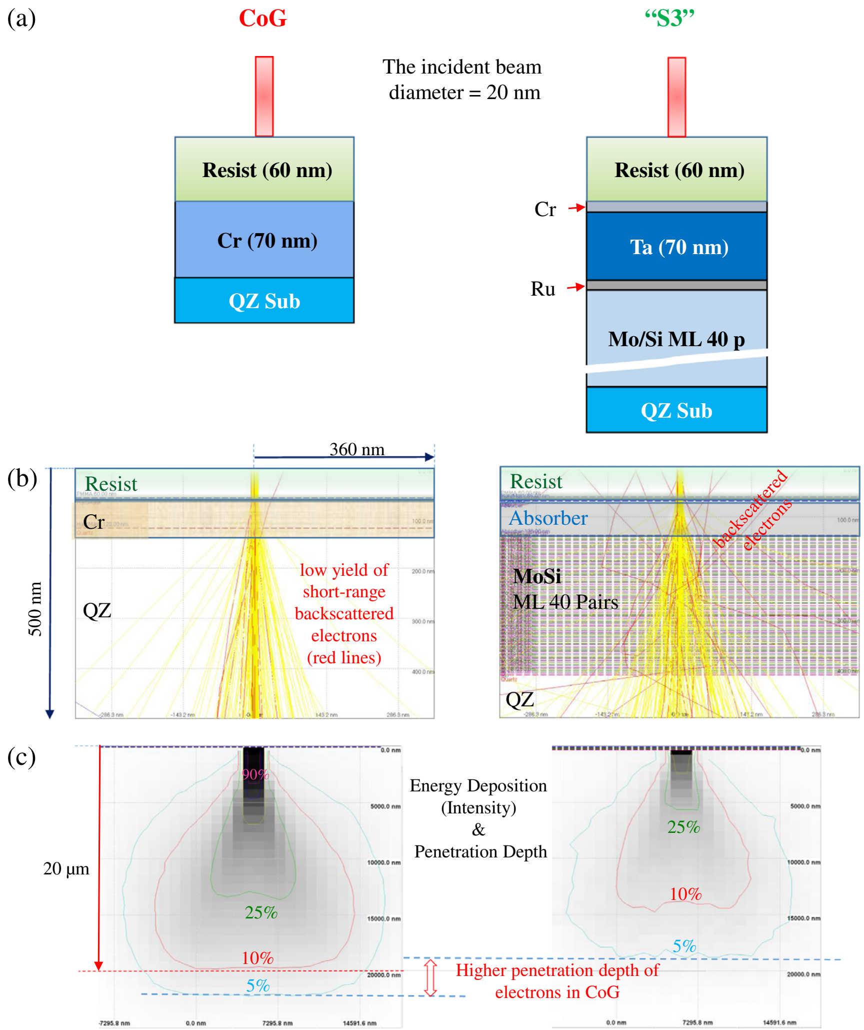

Fig. 2 Comparison between the e-beam scattering behaviors (b), (c) of a standard CoG substrate and the EUV mask coated with the same 60-nm-thick resist (a).

down energy approximation model for the inelastic scattering, accurately tracking trajectories of any electrons above ∼500 eV.[16]

The traditional statistical models assume all forms of deposited electron energy contribute equally to the exposure events. In the more advanced Direct Monte Carlo (DMC) model,[17] the four scattering events (elastic, ionization, excitation, and plasmon generation) are treated separately.[18]

However, in these models, the generation and the impact of SE are not included.

The generated low-energy SE contributes mainly to the density of the radiation chemical changes in polymeric resist as a result of a cascade process that diffuses out from the original impact point of electrons and determines the ultimate resolution of the resist exposure.[11]

Very low-energy SEs generated through Auger transitions and cascades have much higher inelastic collisions probability, causing more local radiation effects in the resist.[19] The detailed process of radiation reactions in the resist is not considered here. All of these models assume all forms of deposited energy contribute equally to the exposure events and the detailed process of exposure reactions is not taken into account. The number of radiation events created by the deposited energy in the resist is also still unknown. Thus, these models do not give any information on local chemical processes in the polymer resist and do not include anything about the spatial extent of the interaction as well. Therefore the energy deposition profile resulting from the Monte Carlo simulation (Fig. 2) cannot be immediately related to the developed final resist-relief pattern cross-sectional shape from the experiment because this result does not precisely predict

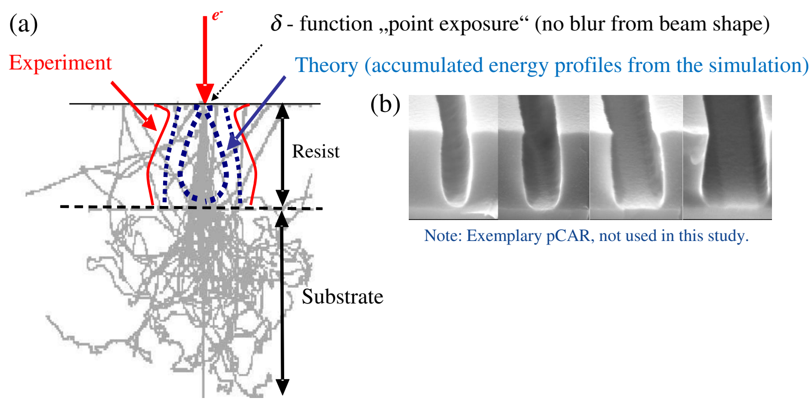

Fig. 3 (a) The discrepancy between the calculated absorbed equal-energy density contours in resist and (b) experimental cross-sectional top-down resist-space profiles captured by XSEM written with the same exposure dose and processed under different development conditions.

the experimental observations, as shown in Fig. 3. Thus, this model does not represent the effects of the lithographic process. The main reason is the non-linear behavior between the simulated equal energy density contours [Fig. 2(c)] and the density of the radiation-chemical molecular changes i.e. the latent image, in the polymer resist volume. Yet this is exactly the cause of the necessary chemical differentiation between exposed and unexposed areas in the resist volume that finally leads to solubility changes in the development process (Fig. 3).

2.2 *Energy Coupling Problem*

From an energetic point of view, the most interesting question concerning an e-beam imaging system is to understand how much of the delivered intensity is transformed to effects determining the development of a pattern in resist.

In the case of complex chemically amplified-resists (CAR), the situation is more complicated because the quantum yield of interest is not a simple chain-scission or a crosslink. The multiple-step-like process in CARs starts with the dissociation of the photo-acid generator (PAG) and the production of acid that catalyzes during the post-exposure bake (PEB) reactions responsible for providing resist contrast. One of the main hurdles is calculating acid diffusion exactly and the resulting impossibility to localize the radiation event precisely enough. There are still fundamental problems in the simulation of processes such as acid production and acid diffusion that have to be solved before starting with adequate modeling. Consequently, higher-level quantitative complete models that can predict a much wider range of phenomena must be developed. These have to incorporate some main behavioral relations that describe:

i. generation of radiation-chemical events as a response of the resist material to the electron irradiation together with the thermo-hydro-kinetics of the development process, tempering, acid diffusion, and outgassing etc.
ii. long-range resist-related factors depending on local pattern density (PD) and the pattern size, such as develop-loading and chemical flare.[20]

2.3 *Resist and Development*

Development is one of the most critical steps in EBL where the real 3D resist-relief pattern will be created. This is a highly nonlinear process in the sense that equal increments of AEDD do not lead to equal increments (positive tone) or decrements (negative tone) of the dissolution rate of resist. A true image optimization algorithm must include these resist-related nonlinearities (resist-related proximity effects) to predict the final resist profile.

The resist-developer interaction determines the rate of dissolution of the resist in the solvent along with the creation of the final 3D-shape and the CD-control. Moreover, the dependence of the development rate on the pattern size and the PD (developer-loading) was also observed.[21,22] For narrow lines, especially those <30-nm wide, the critical energy rises, meaning that in this case the rate of development decreases. The explanation is based on the aggregate-extraction development assumption described by Yamazaki et al.[23] For patterns narrower than the diameter of the aggregate, the aggregates have to be broken up in the development. This and other possible local dissolution variations[24] can explain the slower rate of development with a stochastic induced distribution of small pattern failures such as necking, bridging inside narrow patterns, or random missing of tiny contacts in dense arrays.[25,26] Consequently, we also have to be very careful about how we determine the proper dose for a given nano-pattern. Thus, in nano-structuring, apart from all previously mentioned effects, we also have to take into account the thermo-mechanical factors, like stress in the resist features[27] (e.g., resist shrinking, pattern collapse phenomenon, and resist adhesion to the absorber surface).

To summarize, a complete development model relating to molecular changes of dissolution is extremely complex. The radiation-chemical process may lead to various energy relaxation paths corresponding to different by-products.

Therefore, in the following text, experimental methods to determine the PSF, characterizing the complete lithographic process including the resist behavior under all pre- and post-exposure processes are explained and outlined.

2.4 *Experimental Methods for the PSF Parameters Determination*

The exposure correction algorithm itself is based on an appropriate physical model that can describe all observed effects correctly. This modeling becomes the bridge between the layout design and the optimized writing method of individual patterns.

For precise correction of the pattern degrading effects in EBL, it is important to determine the PSF-parameters with sufficient accuracy. Generally, it is not recommended to use the PSF numerical parameters estimated from the AEDD calculations resulting from, for example, the Monte Carlo simulation. In such a way, calculated energy deposition profiles in resist, due to the electron scattering, may not account for all significant point spreading effects appearing in the lithography process. This calculation only approaches realistic values. The real values are typically different because, apart from the scattering of electrons, additional resist processes as mentioned before and tool-dependent effects[28] (e.g., writing strategy, effects contributing to the resulting beam quality) influence these highly sensitive numerical parameters.

In conclusion, there is no available solution at the moment that directly determines the universal shape of the PSF for a given process. An experimental method of estimating PSF in general, needs to follow the following steps:

i. choose an appropriate physical model that can analytically describe the process;
ii. design and exposure (without any correction) of specific tests containing well defined representative patterns;
iii. precise CD-measurements in specified points on representative test-pattern;
iv. numerical analysis of measured data sets;
v. extraction of physically meaningful numerical parameters of the model from the difference observed between defined and obtained patterns.

Several diverse exposure optimization approaches and techniques have been developed in the last years.[29] The accuracy of the correction strongly depends on several conditions. Small pixel sizes are necessary to obtain an accurate correction. However, convolving large layouts containing small feature sizes and using small pixels with the PSF will give unacceptably long computation times. This causes the correction problem to be continually more difficult. Therefore, the main issue in all existing approaches is the trade-off between both (i) required accuracy, to maintain CD-linearity control, and (ii) computational efficiency, to handle large volumes of data fast, but keeping the resulting on-line run-time data in a reasonable limit.

Great efforts have been taken to develop quick and easy methods for the numerical determination of highly process-customized input parameter sets required to determine the exposure correction algorithms. The exposure distribution is most commonly approximated as a linear combination of two Gauss functions represented with only three parameters characterizing the forward scattering range (α), the backward scattering range (β), and the ratio of the backscattered to the forward scattered exposure intensity (η), as introduced in Ref. 30. Such a 2-Gauss PSF, representing this complex physical process, is adequate for some materials and is usually chosen for convenience and benefits in easier mathematical handling. Going to higher resolution and pattern fidelity, experiments often show significant departures from these assumptions. The distributions of energy deposited in certain resists on certain materials cannot be well represented by a simple sum of only two Gaussians. More complex PSF [e.g., combination of weighted multiple Gaussians[30] (Eq. 1) and/or other functions] must be used to assign exposures properly.

$$f(r) = \frac{1}{\pi(1+\sum \eta_i)}\left[\frac{1}{\alpha^2}\,\exp\left(-\frac{r^2}{\alpha^2}\right) + \sum \frac{\eta_i}{\beta_i}\,\exp\left(-\frac{r^2}{\beta^2}\right)\right]. \tag{1}$$

While α, β_i, and η_i are useful parameters for estimating exposure effects, accurate correction for arbitrary patterns requires detailed knowledge of the exposure-response due to the entire EBL process. Also, the extracted parameters approximate physically reasonable values and should correlate with those obtained from theoretical models.

To optimize the exposure and correct for all undesirable image blurring, it is necessary to determine the exposure intensity distribution and the resist response to this distribution, i.e., the integral distribution of radiation-changes of a single picture element, "pixel," of a predetermined size in the resist. The methods of evaluating the point exposure distribution are accounting for all scattering and other point spread effects, even if they are not fully characterized individually. The data sets obtained from careful measurements allow a fine calibration of the PSF input-parameters for a defined e-beam direct-write process. However, it is essential to verify whether the used corrector (exposure optimization software) will work satisfactorily, i.e., if it will be able to calculate and assign the required dose (number of electrons per area) to each pattern detail using the obtained parameter set. Special care must be taken to synchronize both the algorithms used in the correction and the algorithms used in the parameter extraction method (used exposure model) to obtain the required results after correction. Thus, the parameter extraction algorithms should work under the same model concept as used in the proximity effect correction (PEC), i.e., both algorithms must use the same model.

The highly conformal MBMW resist-patterning process needs to successfully combine the absorbed intensity distribution from the electron scattering in the resist/substrate stack, as well as the consecutive radiation-chemical effects induced by the electron energy spread together with the nonlinear dissolution behavior of the resist in the development process. It is difficult to calculate the exact relative contribution of these factors separately, but their overall effect can be holistically modeled by the analytic process-PSF for a given resist.

The real extent of the native pattern deformation depends strongly on the nature of the substrate system composition.

2.5 *Design of Experiment*

Our study was performed on a traditional CoG mask [Fig. 2(a)] and a set of selected exemplary EUV stack systems prepared at HOYA (Fig. 4). A CoG mask type has a similar resist response as the current advanced phase-shift-mask blanks from HOYA (Fig. 4), which can be characterized

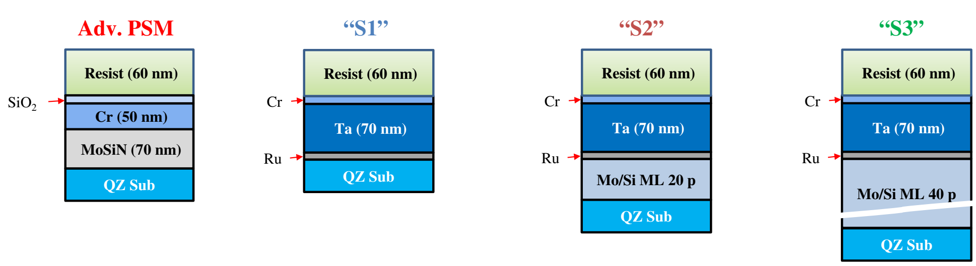

Fig. 4 Schematic of used samples prepared by HOYA identically coated with 60-nm-thick pCAR from FUJIFILM.

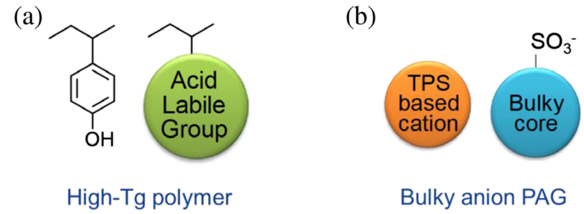

Fig. 5 Key components of the used pCAR: (a) high-Tg polymer and (b) bulky anion PAG.

also with a simple 2-Gauss PSF. Studied EUV masks had identical Ta-based absorbers coated with a thin Cr-based hard-mask layer and differed in the reflective MoSi Bragg mirror ML composition: no Bragg-mirror (S1), 20 ML pairs (S2), and ML 40 pairs (S3) of MoSi reflective bilayers.

The FUJIFILM resist used on our masks is a positive-chemically amplified resist (pCAR) designed for advanced EUV mask manufacturing and exposure on the MBMW tools. The resist is composed of a high-glass transition temperature (high-Tg) polymer and a bulky anion PAG. These are the key components to control acid diffusion and resist profile (Fig. 5).

All masks were coated with identical pCAR provided by FUJIFILM prepared with the same coating process and identically developed with an upgraded Suss ASP-5500 Track. Exposure was performed on the IMS MBMW ALPHA tool in Vienna using 20-nm beam size and total current density of 1 $\mu A/cm^2$. After-development inspection (ADI) was performed with Advantest E3640 CD-SEM. To reduce resist shrinkage during measurement in CD-SEM, the accelerating voltage of the scanning electron beam was 1200 V with a low probe current of just 7 pA, averaging rate of 32 and electron beam scanning mode switched to frame scan, a functionality of Advantest's CD-SEM, which distributes beam scans over the inspected area field of view in a way to reduce surface charging. An accelerating voltage of 1200 V allows electrons to penetrate through resist coating and be captured on grounded metal layers of the absorber, in our case of the EUV mask-stack.

The mask-sets were exposed with a set of test patterns under specified process conditions for several exposure doses, at first without any correction. The tests aimed to determine the specific resist response to the exposure of the resist coated mask stack. The generically developed resist contour placement shift from the defined points was precisely recorded and followed by the model-based analysis of the measured data. These measurements are the target values for our process model calibration. Obtained numerical input model-parameters then allow matching the calculated pattern contour-placement variation from simulation to that obtained directly from the measurement.

Under the assumption that the EBL process is linear and space/time-invariant, e.g., that every exposure-pixel linear superposition holds for the exposure (case of multi-pass writing), the resulting contours at any location (x, y) for an arbitrarily exposed pattern (inside and/or outside the exposed area) can be calculated by the two-dimensional convolution between the exposed pattern and the PSF in the corresponding resist depth level.

Fine-tuning of the numerical PSF parameters allows achieving the best possible reconstruction of exposure effects by simulation and is the key to building an accurate process model. The observed variations of resist-pattern contour placement can be then predictively simulated depending on the location of all exposed patterns in the neighborhood. Consequently, after inserting the well-fitted PSF parameters into the model, the simulation should show the same tendency of pattern geometry variations as obtained from measurements, i.e., the lithography process has been calibrated and matched to the model. Accordingly, if the PEC software of the MBMW-tool is working under the same model as used in our simulation and if controlled by the experimentally obtained process-tailored numerical PSF parameters, the writing process should provide a proper exposure correction of the native parasitic pattern-distortion effects. Thus, in addition to the neatly calculated exposure intensity distribution, the resulting holistic model also includes the whole process and tool-dependent effects. These parameters were later on used in the simulation tool to confirm observed behavior.

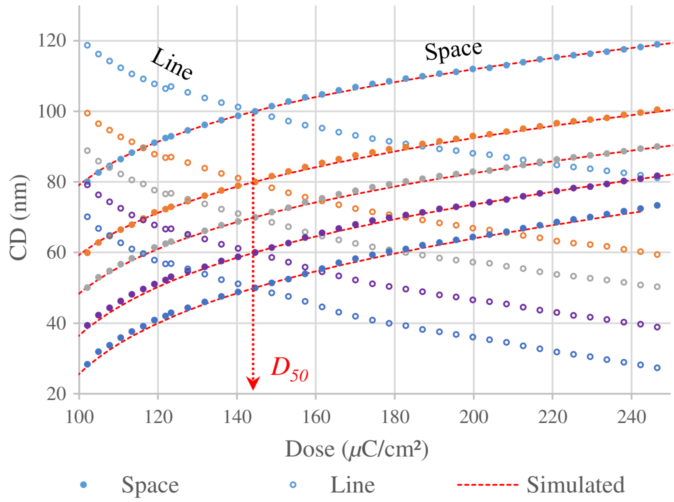

Fig. 6 Illustrates the procedure of base dose (D_{50}) estimation. The graph shows the measured lines and spaces with 50/60/70/80/100 nm hps in the middle of large gratings exposed in an EW with a fine dose-step. D_{50} is defined as the optimum dose when the measured width of the line and space in the grating center is identical (crossing points). We usually take the estimated D_{50} as an anchor value to normalize the applied dose to a dimensionless quantity. This is essential that the D_{50} value is constant for the whole resist process analysis.

2.6 *Base Dose*

Base dose is the main numerical lithographic parameter and is used as the normalization factor in modeling and the exposure corrections and is a constant for a given process.

Estimation of the base dose (D_{50}) is derived from the evaluation of width variations in the central region of large periodic (1:1) line-space (L/S) patterns written with different hps in an exposure wedge (EW) with fine dose-steps through the optimum up to higher dose values without any correction (Fig. 6). The size of the L/S array is dependent on the e-beam energy used. The long-range scattering parameter (β) for 50-keV electrons and the CoG mask is $\sim 10\ \mu$m.

For IMS MBMW systems, the working area of approx. $82 \times 82\ \mu m^2$ suffices well for this requirement. Measurements of lines and spaces are performed in the center of this L/S pattern block.

The measured results of the CD to Dose measurement are shown in Fig. 6 with a specific Dose slope. Experimental base dose determination is then the crosspoint of $CD_{LINE} = CD_{SPACE}$

2.7 α, β_i, *and* η_i*—the Main PSF Parameters*

The main task is to search for reasonable numerical β_i and η_i process-PSF-values required for the next simulation steps. The optimum values allow reconstruction of the real situation with the experimentally obtained contour shape of the resist pattern.

The β_i and η_i values significantly and precisely determine the final resist response to the dose assignment over a large area of interacting and non-interacting patterns in both clear and/or opaque modes, respectively. These parameters are sensitive to the resist/substrate material composition and the pre- and post-exposure processing. The simplest method of determining the resist response to the applied dose is the measurement of resist pattern contour shift by varying the exposure dose.

We used this method based on numerical analysis of the measured linewidth variation versus exposure dose (Fig. 7). The dose increases in fine steps from the smallest reasonable value up to high values ($\sim 10\times$ the optimum dose) to directly visualize the whole effect of the backscattering together with all additional process impacts. Measured data are plotted as a line-width versus dose chart, normalized to base-dose and nominal target width. Figure 7 shows a typical trend of an experimentally measured contour shift in the resist of an exposed isolated wide line. The curve behavior represents the resist response to the backscattering together with all additional

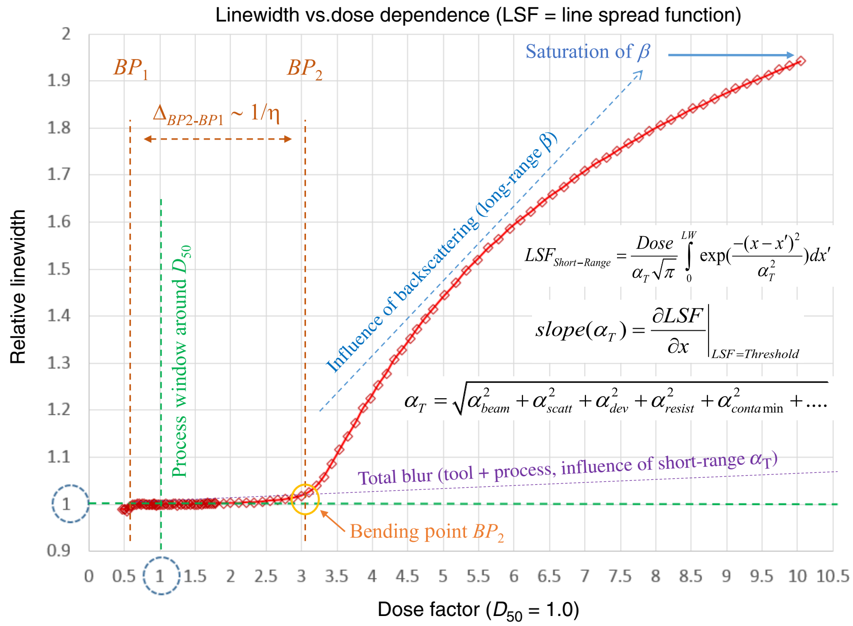

Fig. 7 Typical line-width variation of a wide line-pattern exposed with increasing doses from under- to a strong over-exposure, which allows visualizing the resist-response to the backscattered electrons going up to the saturation. The chart is normalized to base dose (D_{50}) and nominal line width.

process impacts, including process window around the base dose (D_{50}). Total blur is the slope of the linear part of measured response, the influence of backscattering due to long-range β-parameter with saturation at high overexposure, and the weight (η) defined by the length of the linear part of the curve between two bending points (BPs). Assuming the impact of the forward and backward scattering contributions to be Gaussian, we try to physically explain this behavior. Analysis and reconstruction of the measured curve allow the extraction of the numerical deviations of the long-range Gaussian (β) and approximate its weight (η). β and η parameters are used to develop the first exposure model to predict the resist pattern contours.

It is worth noting that even small deviations in the resist processing steps may lead to significant changes in the linewidth versus dose dependency and thereby to changes in PSF parameter values for unchanged resist/substrate materials and exposures.

The estimation of the shortest-range PSF parameter α, responsible for the inherent resolution capability of the litho-system, over the important distance scale below 20 nm, is more challenging and the exact numerical values can be determined only from careful measurements on fine-line patterns where resist metrology will get increasingly complicated. The most difficult features to correct are the small structures with sizes under 100 nm such as square holes, contacts with adjacent corners, closely spaced narrow lines, and jogs. If the test pattern primarily contains such small features and there are no large patterns in the close neighborhood (test pattern is small compared to the range of backscattering), the backscattering effect plays only a minor role in the exposure correction process. Thus, if the PD is small (integrated background dose is low), the optimization in the nanolithography requires mainly short-range corrections (resist, beam aberrations, and the total process blur).

Blue dots on Fig. 8 show CD measurement of fine line patterns at various doses. The resulting measured Dose Slope is specific for the given process. Measured data are numerically analyzed to extract the standard deviation of the short-range Gaussian α. Dashed lines represent reconstructed data by simulation with various α-parameters, which take into consideration long-range and eventually mid-range parameters. The red-dashed line for $\alpha = 17$ nm (corresponding to total blur $\sigma \sim 12$ nm) shows the best fit. As the chart illustrates, the method is very sensitive. Even a very small change in α is well resolved in the sub-nm range. As shown in Fig. 9, small changes in α-value (α—directly related to the total blur) contribute to the resist image formation. Higher values fundamentally degrade the features, cause image blur, and deteriorate the obtained

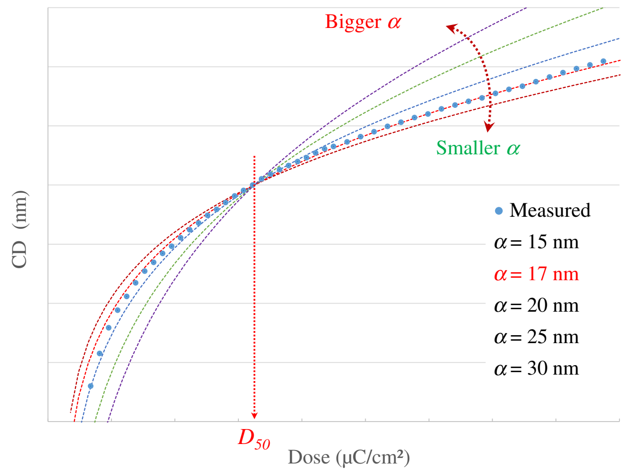

Fig. 8 Illustration of the sensitivity of the short-range α-parameter to the analytical reconstruction of the measured dose-to-line dependency for 100-nm wide line (blue dots) if the rest of all other PSF parameters (already determined before) remain constant.

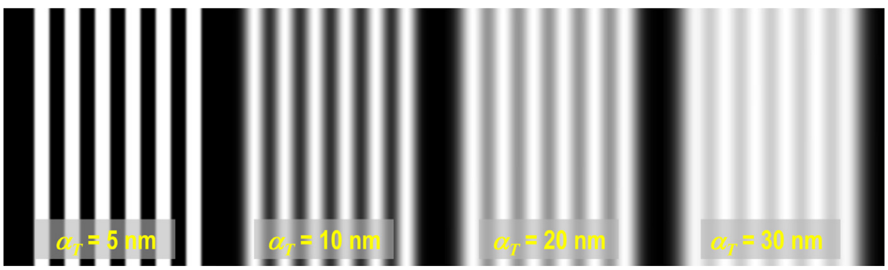

Fig. 9 Aerial image of nested lines simulated with various α.

pattern.[31] The higher the α-value, the lower the ultimate accessible resolution and as a direct consequence more aggressive dose-correction in the whole write procedure will be necessary.

As a cross-check and for the final fine-tuning of the process parameters, it is recommended to use a verification test-pattern exposed with exactly known varied pattern densities. For this purpose, we used large arrays of various L/S rates. The goal here is again to reconstruct the measured native deformation of exposed feature details under changed local pattern loading by appropriate process simulation, which should reflect actual process behavior.

The next specific pattern we are using in the resist screening process dose-dependency is the EW applied in the direct measurement of the resist response to large-area exposures under specified pre- and post-exposure conditions. The EW layout, as shown in Fig. 10, consists of a set of exchanging large-area pads ($>60 \times 60$ μm^2) exposed with individual doses assigned in an

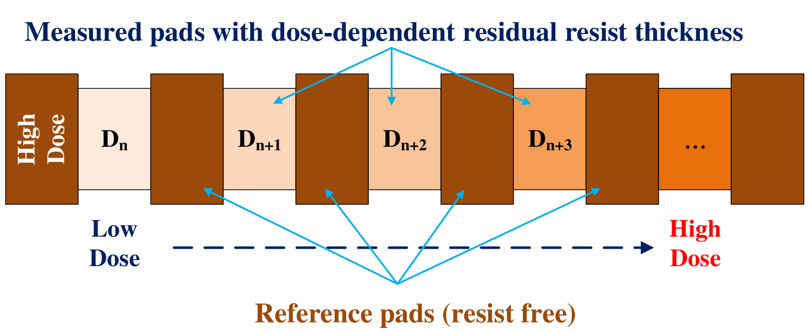

Fig. 10 Schematic illustration of EW pattern layout.

ascending order starting from under-exposure to over-exposure with fine dose-steps. Each pad exposed with a specific dose is surrounded from both sides by over-exposed and fully developed pads as reference planes. This configuration allows the measurement of the residual resist thickness responding to the individual dose using a profilometer in contact mode. The measured results are roughly independent of the e-beam writer parameters itself (beam size, beam blur, astigmatism, focus plane, and butting) and also of some process parameters (e.g., dose latitude) or metrology offsets. Figure 11(b) shows the dependency of the residual resist thickness (dissolution properties of resist) to the applied exposure dose within large-area exposures. This directly provides the resist contrast curve under the specified post-exposure process.

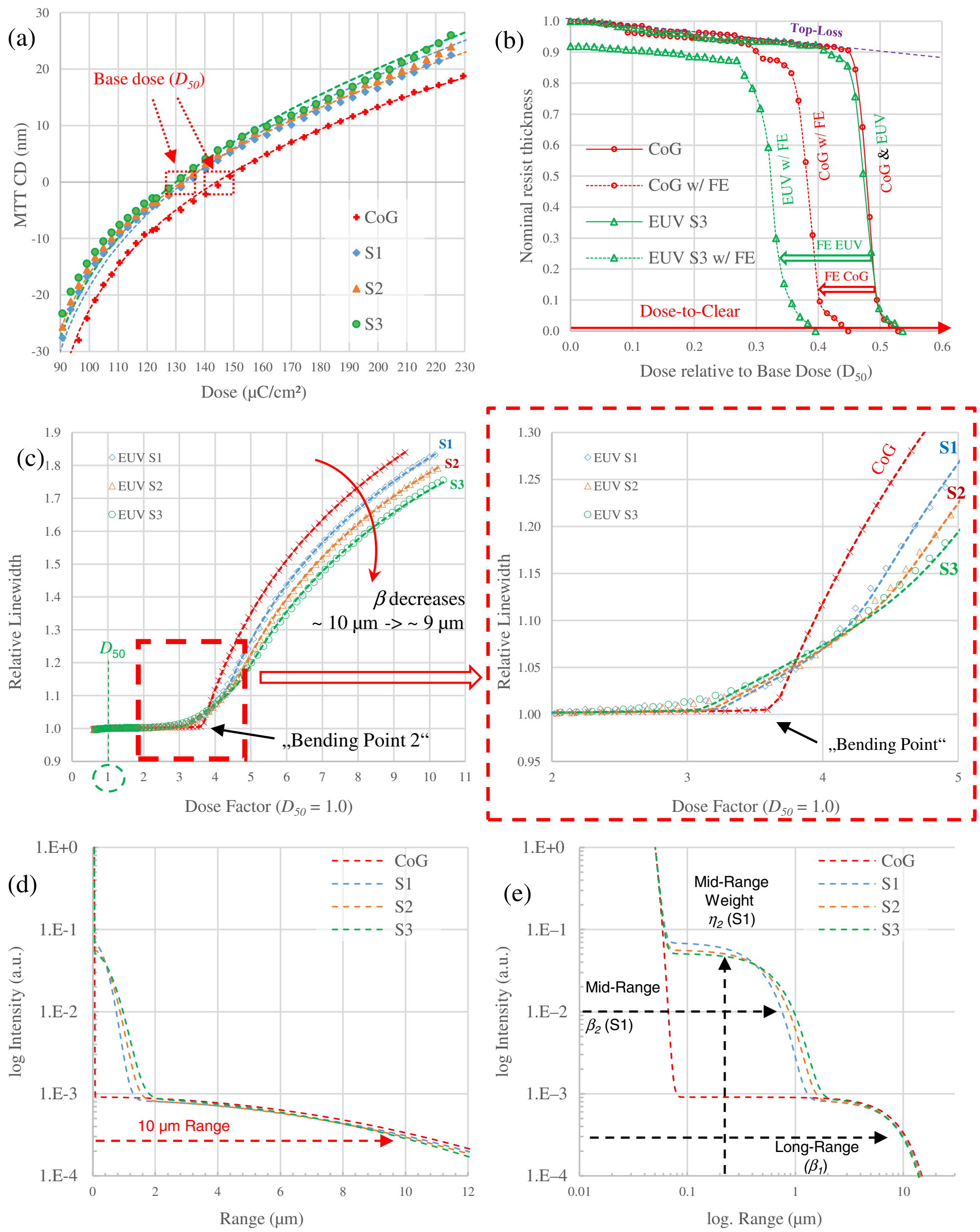

Fig. 11 (a) Dose slopes of (1:1) L/S test pattern with the highlighted Base Dose (D_{50}); (b) sensitivity (characteristic) curves of the analyzed pCAR on CoG and the EUV S3 samples w/o and with FE plotted in dose relative to D_{50} obtained from (a); (c) resist pattern-contour shift dose-dependency behavior for different EUV-stacks (S1, S2, and S3) compared with CoG substrate; (d) calculated process-PSFs for four different mask stack compositions; (e) log-log presentation of the PSFs from (d).

Along with the resist dark-erosion and "top-loss," the quantitative analysis of the measured data yields the dose at which the resist fully develops and is called dose-to-clear (D_2C). The large area of the pads also means the pads are already completely saturated from the short- and long-range electrons. In addition, the test is also sensitive to very-long-range fogging-electrons. The result from this test shows all tool/process effects in the resist, so the pattern can be effectively used for accurate local and/or global process stability monitoring and mapping as well.

3 Results and Discussion

Figure 11 shows the experimentally measured and analyzed substrate-stack specific dependent lithographic parameters. Figure 10(a) shows the resulting CD change to the dose variation of (1:1) L/S pattern as mean-to-target (MTT) versus exposure dose. The dose where MTT $= 0$ is considered the base dose (D_{50}). The slope of lines around the base dose directly relates to the total process blur (short-range parameter α).

Results from a cross-check using our EW-test are shown in Fig. 11(b). Measured residual resist thickness data normalized to the original resist thickness are plotted as a function of dose relative to base dose (D_{50}) derived from Fig. 11(a). With increasing dose up to ca. $0.4 \times D_{50}$, the resist thickness is linearly decreasing, creating the so-called top-loss. The exact knowledge of the top-loss dependence allows calculating the resist pattern height loss modulation dependent on local PD changes (see Fig. 12). This effect directly contributes to the 3D resist-image formation causing local image blur and deteriorating the contrast quality of the resist profile. A rapid change in resist thickness occurs at doses close to $0.5 \times D_{50}$. This part of the curve characterizes the contrast of the resist. The steeper the thickness change, the better contrast of the resist and the better the resist function as a threshold detector. Plotting a tangent to the steepest part of the resist sensitivity curve will point to the D_2C at which the resist clears the central region of the exposed pad. The D_2C is achieved at dose approximately half of the base dose (D_{50}). The two parallel dashed curves to the left in Fig. 11(b) represent the change of the same resist response shift to the long-range fogging effect (FE) for the worst case of a 100% large-area PD. The left curve belongs to the sample (S3) containing the complete EUV-stack of 40 ML pairs whereas the curve in the middle shows the resist response of the standard CoG sample.

Figure 11(c) shows the linewidth vs. dose functions obtained from measurements of line-patterns over a very wide dose range to collect as many backscattered electrons as possible into the evaluated pattern. Measured data are normalized to base dose (D_{50}) and nominal target line-width. Dashed lines represent the mathematical reconstruction. The strong overexposure visualizes the resist-response mainly to the important mid- and long-range scattering around the BP_2. Also, the form of this function for each mask stack is distinctive. Even small changes in the composition of the sample can be distinguished. We observe a visible difference in the long-range properties of the EUV samples. With the increasing number of EUV mirror MLs

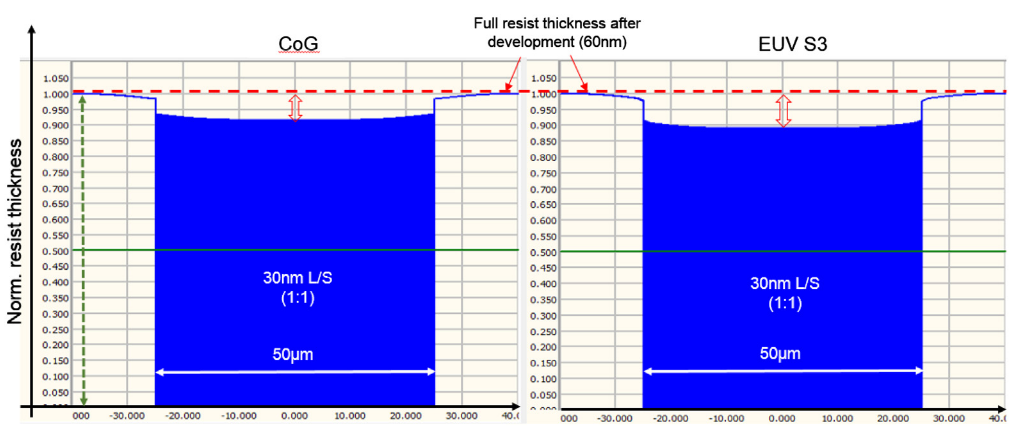

Fig. 12 Simulated resist thickness modulation (height loss in resist profile) across the center of a 50 μm $\times$ 50 μm array of 30 nm (1:1) L/S processed in 60-nm-thick pCAR coated on standard CoG (left) and EUV-Mask (S3), which contains a complete absorber with 40 ML pairs of MoSi stack.

Table 1 Extracted process PSF parameters for the given pCAR response on four different mask-stacks.

	CoG	EUV S1	EUV S2	EUV S3
Absorber	Chrome	Only absorber	w/ 20 ML	w/ 40 ML
Base dose	145	133	132	130.5
Tailored PSF process parameters				
α (nm)	15	19	19	19
η_1/β_1 (μm) long-range	0.40/10.00	0.39/10.00	0.38/9.77	0.37/9.33
η_2/β_2 (μm) mid-range	—	0.09 /0.53	0.11/0.65	0.13/0.74

(0 → 20 → 40 ML for samples S1, S2, and S3) long-range β-parameter shortens from 10 μm down to ~9 μm. As can be seen from Fig. 11(c), the mid-range scattering effect is only marginally present in the CoG mask, thus it can be reconstructed using a 2-Gaussian PSF. In the case of EUV masks, the situation is different because a significant amount of exposure intensity is found in the transition region between the forward- and backscattering [Figs. 11(d) and 11(e)]. The long-range scattering of the S1 sample (w/o MoSi ML) is similar to the CoG mask, whereas the EUV absorber increases the mid-range scattering effects. The addition of Bragg-mirror layers to EUV masks S2 (20 MoSi ML-pairs), and S3 (40 MoSi ML-pairs) affect the mid-range parameters. The mid-range (β_2) and the ratio of mid-range scattering (η_2) are rising. Table 1 presents the sets of the obtained process-PSF parameters corresponding to the four used masks.

Table 1 shows the extracted values for the calibrated process PSFs from Figs. 11(d) and 11(e). The numerical analysis of measured data from the CoG sample allows for a simple 2G (2-Gaussian) PSF approximation describing and correcting the resist response to the exposure. From the point of long-range backscattering, we see a similar tendency as we observed in Fig. 11(c), the addition of Bragg Mirror (20 and 40 ML pairs) visibly shortens the range of long-range backscattering β_1. Regarding the effects in the mid-range area, Fig. 11(e), this part also correlates well with measurement. Sample S1 (absorber only) already shows a β_2/η_2 mid-range component. Range β_2 extends in samples S2 and S3, which is confirmed with the same

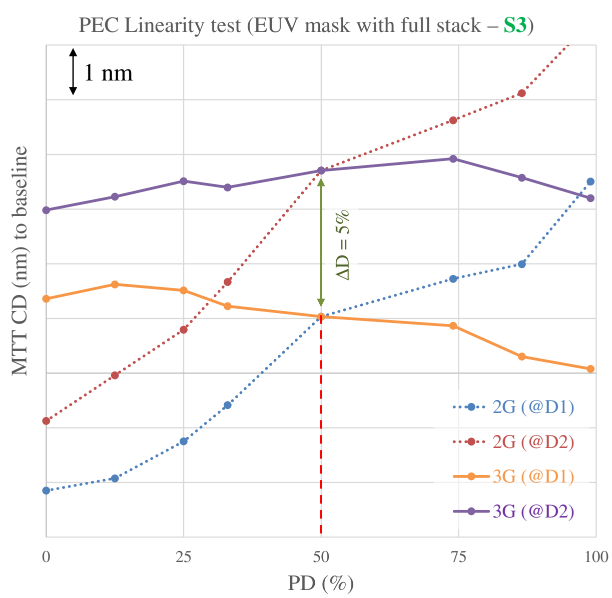

Fig. 13 PEC linearity test. The chart compares CD-linearity response over varying PD of a test pattern corrected using 2-Gaussian and 3-Gaussian PSF correction model on EUV Sample S3 with full 40-ML mirror stack.

tendency from the measurements shown in Fig. 11(c). Comparison of the weighting parameter η_2 is much more complicated due to its high reliance on the correct estimation of the D_{50}.

Process PSF parameters summarized in Table 1 were experimentally validated using sets of exposed PEC linearity tests shown in Fig. 13. Measurements show CD-linearity behaviors over the whole range of pattern densities, using 2- and 3-Gauss PSFs, for two base doses $D1$ (bottom

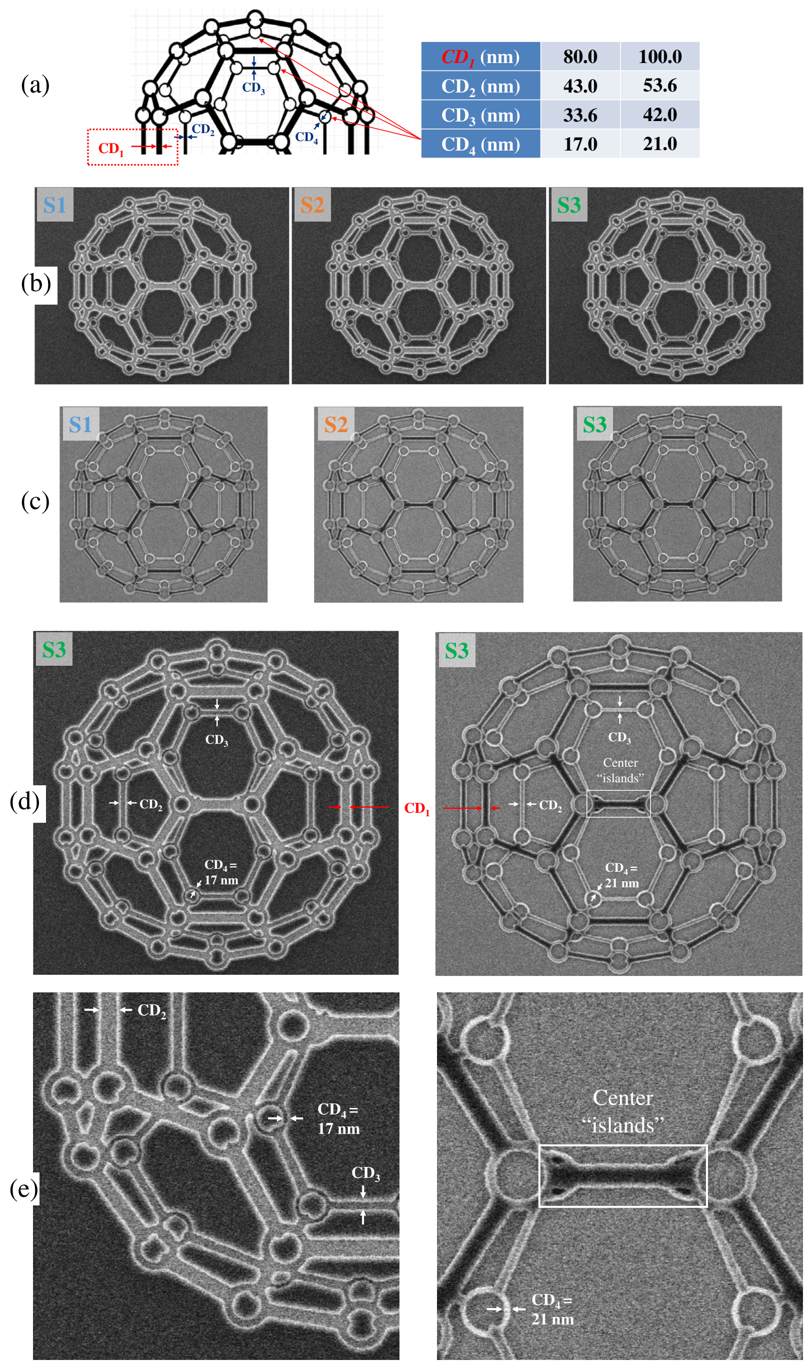

CD_1 (nm)	80.0	100.0
CD_2 (nm)	43.0	53.6
CD_3 (nm)	33.6	42.0
CD_4 (nm)	17.0	21.0

Fig. 14 Mock curvilinear pattern design—Bucky-Ball; (b) CD-SEM images of patterns with reference linewidth CD1 = 80-nm exposed in clear tone on EUV samples S1, S2, and S3; (c) CD-SEM images of patterns with reference linewidth CD1 = 100-nm exposed in opaque tone on EUV samples S1, S2, and S3; (d) SEM image with details of clear tone pattern (left) with reference line width CD1 = 80 nm and pattern in opaque tone (right) with CD1 = 100 nm exposed on EUV sample S3; (e) SEM close-up details of clear (left) and opaque tone (right) patterns.

blue line) and $D2$ (upper red line) differing by 5%. The figure shows the result for EUV sample S3 with a full EUV mirror. The 2G PSF for EUV sample S3 was obtained using mathematical reconstruction from Fig. 10(c). Comparing measured curves on Fig. 13, a visible improvement in CD linearity control is present for the 3G (3-Gaussian) PSF correction model at both doses $D1$ and $D2$. A 3G PSF allows using a wider range of finely tailored dose assignments to each pattern detail, resulting in a larger process window. The positive effect of 3 (or more)—Gaussian PSF correction will be more beneficial in layouts with strongly alternating local pattern densities with fully curvilinear patterns.

Resolution capabilities of the pCAR resist coated on EUV masks with different stack compositions were tested using a mock curvilinear pattern resembling a "Bucky Ball". Its shape is widely known, therefore easy to inspect for any irregularities. The schematic layout of this mock pattern is in Fig. 14(a). We exposed this pattern in a clear and opaque tone, with various scaling and with PEC parameters evaluated for each EUV sample from Table 1. CD-SEM images of the clear tone pattern exposed with a reference line width of 80 nm marked as CD_1 are shown in Fig. 14(b). The smallest rings with a radial cross-section of just 17 nm marked as CD_4 are resolved. CD-SEM images of the opaque tone mock pattern with reference line width $CD_1 =$ 100 nm are shown in Fig. 14(c). A detailed image of the pattern in a clear and opaque tone on EUV sample S3 is shown in Fig. 14(d). Thin rings marked with CD_4 label are resolved with a good line fidelity. The small "islands" highlighted in the center of the opaque tone pattern (right) are also mostly resolved. These non-orthogonal features are in the sub-20-nm region.

4 Conclusion

Various mask-materials were explored using fast statistical Monte Carlo Modeling. Simulations have shown alterations in the absorbed energy distributions of EUV masks with different stacks, which is fully consistent with experimental observations. Even though, we could not directly use the numerical values obtained from the statistical simulation to describe the real process. The described model-based semi-empirical method creates a link between the model-parameters obtained using results from precise direct measurements on the created patterns and the calculated ones using often uncertain fundamental physics. The experiments confirmed tendencies and the fact that each small change in the mask absorber/ML composition requires an adequate writing optimization, i.e. the necessity to adapt the model calibration values to changes in the mask stack composition.

Adequate process parameters were extracted using the described holistic method utilizing data analysis from precise metrology on a set of specially designed test patterns. The obtained parameter set creates the base for solving the inverse problem in the lithography. Further advanced dose-geometry fine computational corrections, such as MPC, allows minimizing the difference between the final- and the ideal image.

This method was successfully implemented into leading-edge mask writing and resist/substrate/tool testing for achieving the 7-nm technology node and below (Fig. 14) at different EUV-mask stacks.

5 Summary

MBMW enables the precise geometry control and faithful reproduction of even ideal curvilinear shapes generated with an appropriate exposure and process margin to finally yield optimum wafer patterning quality.

Acknowledgments

Authors from IMS thank Dr. Hans Loeschner for helpful comments and discussion. We also want to thank SUSS MicroTech Photomask Equipment GmbH for technical support with optimizing resist PEB and tuning the development process on ASP-5500 Mask Process Track.

References

1. F. Abboud et al., "Mask data processing in the era of mulibeam writers," *Proc. SPIE* **9235**, 92350W (2014).
2. I. Bork and P. Buck, "MPC strategies for multi-beam mask writers," *Proc. SPIE* **11177**, 1117707 (2019).
3. M. Chandramouli et al., "Development and deployment of advanced multi-beam mask writer," *Proc. SPIE* **11324**, 113240K (2020).
4. C. Klein, H. Loeschner, and E. Platzgummer, "MBMW-201: The next generation multi-beam mask writer," *Proc. SPIE*, **10958**, 10958OK (2019).
5. T. Hiromatsu et al., "Continuous challenges for next era of lithography," *Proc. SPIE* **11177**, 1117705 (2019).
6. M.-C. van Lare, F.J. Timmermans, and J. Finders, "Alternative reticles for low-k1 EUV imaging," *Proc. SPIE* **11147**, 111470D (2019).
7. H. Mesilhy et al., "Pathfinding the perfect EUV mask: the role of the multilayer," *Proc. SPIE* **11323**, 1132316 (2020).
8. S. Jaiswal, "Enhancing lithographic performance by new EUV photomask materials," *Proc. SPIE* **11609**, 116090F (2021).
9. I. Raptis et al., "Calculation of energy deposition in thin resist films over multilayer substrates," *Microelectron. Eng.* **41-42**, 171 (1998).
10. G. Han and F. Cerrina, "Energy transfer between electrons and photoresist: its relation to resolution," *J. Vac. Sci. Technol. B* **18**(6), 3297 (2000).
11. B. Wu and A. Neureuther, "Energy deposition and transfer in electron-beam lithography," *J. Vac. Sci. Technol. B* **19**(6), 2508 (2001).
12. D.C. Joy, *Monte Carlo Modeling for Electron Microscopy and Microanalysis*, Oxford University Press, New York, NY (1995).
13. K. Murata and D.F. Kyser, "Monte carlo methods and microlithography simulation for electron and X-Ray beams," *Adv. Electron. Electron. Phys.* **69**, 175–259 (1987).
14. M. Dapor, *Application of the Monte Carlo Method to Electron Scattering Problems*, Vol. **186**, Springer Tracts in Modern Physics.
15. D. Drouin et al., "CASINO V2.42– a fast and easy-to-use modeling tool for scanning electron microscopy and microanalysis users," *Scanning* **29**, 92–101 (2007).
16. D.C. Joy and S. Luo, "An empirical stopping power relationship for low-energy electrons," *Scanning* **11**, 176 (1989).
17. M. Kotera et al., "A simulation of electron scattering in metals," *Jpn. J. Appl. Phys. Part 1* **29**, 2277 (1990).
18. H.A. Bethe, "Zur Theorie des Durchgangs schneller Korpuskularstrahlen durch Materie," *Ann. Phys.* **397**, 325 (1930) and H.A. Bethe, J. Ashkin, Experimental Nuclear Physics,. E. Segre Ed., 1, pp. 166-357 (Wiley, NY, 1953).
19. D.S. You, H.M. Li, and Z.J. Ding, *J. Electron Spectrosc. Related Phenom.* **222**, 156–161 (2018).
20. T. Brunner, Z. Chen, and K. S. Scheer, "A new long range proximity effect in chemically amplified photoresist processes: chemical flare," *Proc. SPIE* **5753**, 261 (2005).
21. L.K. Sundberg et al., "Two complementary methods to characterize long range proximity effects due to develop loading," *Proc. SPIE* **7823**, 78230G (2010).
22. J. Kon et al., "Characterization of fogging and develop-loading effects in electron-beam direct-writing technology," *Jpn. J. App. Phys.* **51**, 06FC04 (2012).
23. K. Yamazaki et al., "Novel proximity effect including pattern-dependent resist development in electron beam nanolithography," *Jpn. J. Appl. Phys.* **36**, 7552–7556 (1997).
24. P. De Bisschop and E. Hendrickx, "On the dependencies of the stochastic printing-failure cliffs in EUV lithography," *Proc. SPIE* **11323**, 113230J (2020).
25. H. Yaegashi et al., "Explorations of missing hole defect in EUV patterning," *Proc. SPIE* **11326**, 113260E (2020).
26. S. Nagahara et al., "EUV resist chemical gradient enhancement by UV flood exposure for improvement in EUV resist resolution, process control, roughness, sensitivity, and stochastic defectivity," *Proc. SPIE* **11326**, 113260A (2020).

27. Y. Granik, "Analytical solutions for the deformation of a photoresist film," *Proc. SPIE* **10961**, 109610D (2019).
28. A. Eilert et al., "Multiple exposure on single blank for electron-beam writer characterization," *Proc. SPIE* **10810**, 108101G (2018).
29. P. Li, "A review of proximity effect correction in electron-beam lithography," Mesoscale and Nanoscale Physics [cond-mat.mes-hall], https://arxiv.org/abs/1509.05169 (2015).
30. T. H. P. Chang, *J. Vac. Sci. Technol.* **12**, 1271 (1975).
31. B. Shamoun et al., "Multi-beam mask writer in EUV era—challenges and opportunities," *Proc. SPIE* **11610**, 116100Q (2021).

Biographies of the authors are not available.